

The 2016 Gyeongju earthquake sequence revisited: aftershock interactions within a complex fault system

Jeong-Ung Woo¹, Junkee Rhie¹, Seongryong Kim², Tae-Seob Kang³, Kwang-Hee Kim⁴ and YoungHee Kim¹

¹School of Earth and Environmental Sciences, Seoul National University, Seoul 08826, Korea. E-mail: rhie@snu.ac.kr

²Department of Geology and Earth Environmental Sciences, Chungnam National University, Daejeon 34134, Korea

³Department of Earth and Environmental Sciences, Pukyong National University, Busan 48513, Korea

⁴Department of Geological Sciences, Pusan National University, Busan 46241, Korea

Accepted 2019 January 5. Received 2018 December 20; in original form 2018 June 16

SUMMARY

On 2016 September 12, a moderate earthquake (M_L 5.8) occurred in Gyeongju, South Korea, located hundreds of kilometres away from the nearest plate boundaries. The earthquake, the largest instrumentally recorded event in South Korea, occurred in a sequence of thousands of earthquakes, including a M_L 5.1 event 50 min before the main quake and a M_L 4.5 event a week later. As a case study, we analyse the source parameters of the 2016 Gyeongju earthquake sequence: precise relocations, fault structures, focal mechanisms, stress tensor analysis and Coulomb stress changes. To determine high-resolution hypocentres and focal mechanisms, we employ our temporary seismic network for aftershock monitoring as well as regional permanent seismic networks. The spatio-temporal distribution of events and inverted moment tensors indicate that the M_L 5.1 event and the M_L 5.8 event occurred on two parallel dextral faults striking NNE–SSW at a depth of 11–16 km, and the M_L 4.5 event occurred on their conjugate fault with sinistral displacements. Seismicity on the fault for the M_L 5.1 event abruptly decreased as soon as the M_L 5.8 event occurred. This is not solely explained by the Coulomb stress change and requires more complex processes to explain it. The tectonic stress field obtained from inverted focal mechanisms suggests that the heterogeneity between the intermediate and minimum principal stresses exists along the NNE–SSW and vertical directions. The Coulomb stress changes imparted from the M_L 5.1 event and the M_L 5.8 event are matched with the off-fault seismicity, including that from the M_L 4.5 event. Multifaceted observations, such as Coulomb stress interactions between parallel or conjugate faults and the heterogeneity of the tectonic stress field in the aftershock area, may reflect the reactivation processes of a complex fault system. This study offers a distinctive case study to understand the general characteristics of intraplate earthquakes in multifault systems.

Key words: Earthquake interaction, forecasting, and prediction; Earthquake source observations; Continental neotectonics; Dynamics: seismotectonics; Dynamics and mechanics of faulting.

1 INTRODUCTION

Intraplate earthquakes pose certain seismic hazards and risks as natural disasters, although they are responsible for only 5 per cent of the world's seismic moment release (Chen *et al.* 1988; Johnston 1989; Durá-Gómez & Talwani 2009; Rastogi *et al.* 2001; Wang 2007). Despite their importance in hazard analysis, their general characteristics are not well understood (Gangopadhyay & Talwani 2003; Talwani 2014). It is widely accepted that intraplate earthquakes are caused by the tectonic forces transmitted from plate boundaries and are located in pre-existing zones of weakness, such as failed

rifts (Sykes 1978; Talwani & Rajendran 1991; Zoback 1992; Bodin & Horton 2004; Tavakoli *et al.* 2010). However, this hypothesis has not been clearly verified because some studies have reported that intraplate earthquakes occur regardless of faults with surface expressions (Ferreira *et al.* 1998; Assumpção *et al.* 2004). Furthermore, the rarity of the surface extension of fault ruptures makes it hard to observe the causality (Adams *et al.* 1991). Our understanding of intraplate earthquakes has advanced as many seismographs are installed in intraplate regions and diverse approaches for array networks are developed (Talwani 2014; Bianchi *et al.* 2018; Matos *et al.* 2018; Ross *et al.* 2018; Soto-Cordero *et al.* 2018).

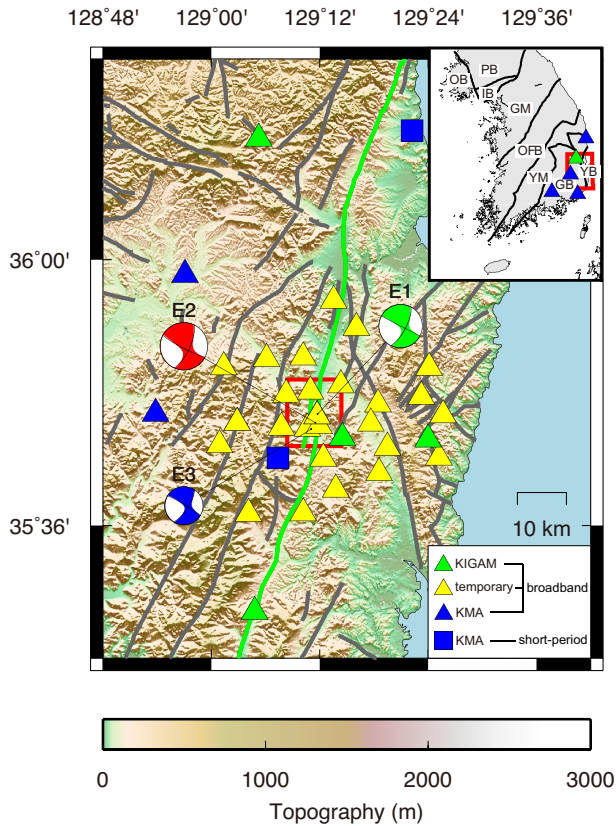


Figure 1. The distribution of the stations used for the detection of events and determination of their locations, magnitudes and focal mechanisms. The three major events (E1, E2 and E3) are shown with their moment tensors obtained from the low-frequency waveform inversion method. The two faults with surface expressions near the main shock are denoted as green lines. Other faults and lineaments with surface expression are shown as dark grey lines. Six broad-band sensors operated by the Korean Meteorological Administration (KMA) and Korea Institute of Geoscience and Mineral Resources (KIGAM) are illustrated as green and blue triangles, and the 27 temporary broad-band sensors are represented by yellow triangles. Two short-period sensors from the KMA are denoted as blue squares. The red box corresponds to the regions in Figs 2(b) and 3(a). Major geological units are separated with black lines in the inset: PB (Pyungnam Basin), OB (Ongjin Basin), IB (Imjingang Belt), GM (Gyeonggi Massif), OFB (Okcheon Fold Belt), YM (Youngnam Massif), GB (Gyeongsang Basin) and YB (Yeonil Basin). The box with red lines in the inset indicates the region of the main figure. The five broad-band seismometers shown in the inset are used to determine the moment tensor solutions of the ten selected events.

The Korean peninsula is an intraplate region located ~ 800 km away from the Ryukyu and Nankai trough. According to an event catalogue published by the Korea Meteorological Administration (KMA), only 10 earthquakes with $M_L \geq 5$ have been instrumentally recorded since 1978 (So *et al.* 2016). The largest among them, a M_L 5.8 earthquake in Gyeongju, South Korea on 2016 September 12, produced strong coseismic ground shaking, which was sufficient to be felt throughout South Korea (Hong *et al.* 2017). The event happened in the Gyeongsang Basin, where there are several systematic fault sets with surface expression, such as the Yangsan and Gaum Fault Systems (Figs 1 and 2a, Chang 1977; Hwang *et al.* 2008; Han *et al.* 2017). The 2016 Gyeongju earthquake sequence started from a M_L 5.1 event that ruptured 50 min before the M_L 5.8 event, and thousands of earthquakes, including a M_L 4.5 aftershock on September 19, occurred in the sequence (Kim *et al.*

2016b). Hereafter, for convenience, we refer to the three events of M_L 5.1, M_L 5.8 and M_L 4.5 as E1, E2 (the main shock) and E3, respectively. From the distribution of the hypocentres and inverted moment tensors of the three events, it has been demonstrated that these earthquakes occurred on a deep-seated fault system at a depth range of 10–18 km (Kim *et al.* 2016a; Hong *et al.* 2017; Son *et al.* 2017; Kim *et al.* 2017a,b; Lee *et al.* 2018). In particular, Son *et al.* (2017) delineated two distinct parallel dextral faults striking to the NNE–SSW direction from relocated aftershocks, and Uchide & Song (2018) observed that the inverted finite fault slips of E1 and E2 propagated towards SSW and NNE directions, respectively. A possible correlation between the Yangsan Fault and the Gyeongju earthquakes has been raised because the epicentres are located close to the fault, with 30 km of dextral displacement (Kyung 2003; Kim *et al.* 2017b,c; Lee *et al.* 2018). However, it is difficult to prove whether the deep-seated fault system extends to the surface because the focal depths exceed 10 km, and no surface deformation due to E2 has been reported (Park *et al.* 2018).

In this study, we investigated the source parameters of the Gyeongju earthquakes using a larger data set obtained from both permanent and temporary seismic networks. Our basic goal is to create a more complete catalogue of earthquakes in the vicinity of the mainshock from 2014 to 2016. We located earthquakes detected by an automatic algorithm and resolved the detailed fault segments based on the Double-Difference method. The relative magnitudes of events were estimated from the amplitude ratios with reference events. Long period waveforms and the first motions of *P*-wave polarities were used for moment tensor inversion and focal mechanism determination, respectively. Based on our catalogue, we conducted further analysis, including the consideration of statistical parameters, tectonic stress fields and the role of stress transfer induced by E1 and E2. These multifaceted approaches will contribute to a better understanding of both the reactivation process of interacting complex faults in the aftershock region and the generalized characteristics of intraplate earthquakes within complex fault systems.

2 DATA ACQUISITION

The data used for the detection of events and the determination of their hypocentres, magnitudes and focal mechanisms are divided into two parts: the continuous waveforms recorded at permanent seismic stations and those from temporary seismic stations installed for monitoring aftershocks and analysing detailed source parameters (Fig. 1). Three years of waveform data from January 2014 to December 2016 were gathered from six broad-band and two short-period seismometers within 50 km of the E2 epicentre. For moment tensor determination of the 10 selected events, waveforms recorded at three broad-band stations with epicentral distances greater than 50 km were also collected, and data from five broad-band stations (inset of Fig. 1) were used in the end. The temporary network of 27 broad-band instruments began operation within 2 hr of E1, and we assembled the waveform data through the end of 2016 (Fig. 1). For the epicentre of E2, the data coverage of the eight permanent stations yields an azimuthal gap of 80° and a minimum epicentral distance of 5 km. However, by adding data from the temporary instruments, the two parameters could be reduced to a gap of 32° and a minimum epicentral distance of 0.9 km. Therefore, it is expected that not only can additional events with small magnitudes be detected but also that the source parameters of the earthquakes can be analysed at high-resolution scales using both the permanent and

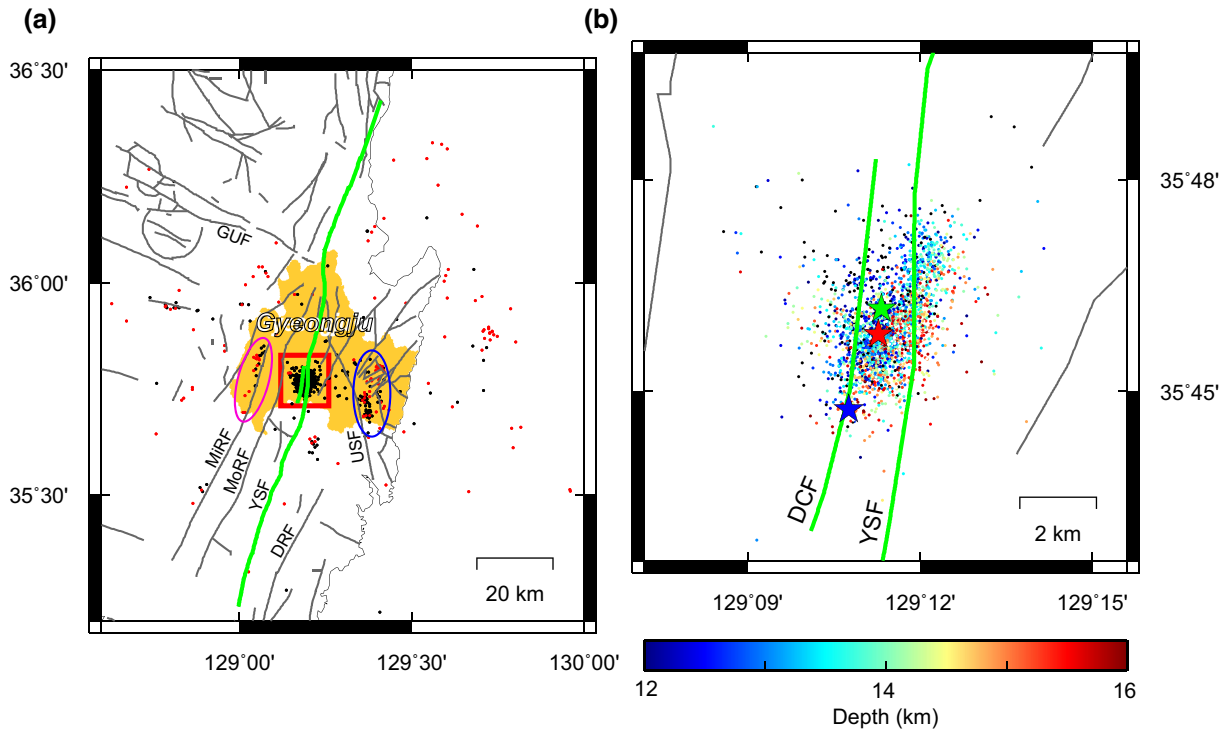


Figure 2. (a) Distribution of the hypocentres calculated from the visually inspected P-phase and S-phase arrival times and (b) a zoomed-in view of the region of interest. The seismicity values before and after the onset of E1 are shown with red and black dots, respectively. The names of major surface ruptures are presented with abbreviations: GUF (Gaum Fault), MiRF (Miryang Fault), MoRF (Moryang Fault), YSF (Yangsang Fault), DRF (Dongrae Fault), USF (Ulsan Fault) and DCF (Deokcheon Fault). The blue circled area and magenta circled area have experienced temporal changes in seismicity (see details in Section 3.2). The red box in (a) corresponds to the zoomed-in region of (b). The green, red and blue stars in (b) are the locations of E1, E2 and E3, respectively. The other symbols match those in Fig. 1.

temporary stations (see details about the temporary seismic network in Kim *et al.* 2016a).

3 HYPOCENTRE DETERMINATION

3.1 Method of analysis

To analyse not only the aftershocks within a few kilometres of the E2 epicentre but also the seismicity changes before and after E1, we applied an automatic earthquake detection method to continuous waveform data and determined their absolute locations using the single difference method (HYPOELLIPSE, Lahr 1999). In order to resolve the spatial pattern of the aftershocks, the earthquakes near E2 were relocated using the Double-Difference algorithm (HypoDD, Waldhauser & Ellsworth 2000). *P*- and *S*-wave phase arrival times were automatically measured from the recursive short-term average to long-term average ratio (STA/LTA) method (Withers *et al.* 1998; Grigoli *et al.* 2013; Woo *et al.* 2017). Then, incorrectly measured phase arrival times were manually inspected to discriminate overlapping events and remove false detections. A regional 1-D velocity model for the Gyeongsang Basin (e.g. Kim *et al.* 2011) was applied throughout the hypocentre determination.

In the process of relocation, the traveltimes differences calculated from 545 024 chosen arrival time pairs as well as those measured from 3840 597 waveform cross-correlation pairs were applied. We tested whether the data obtained from the chosen arrival times distort the relocation results and confirmed insignificant changes in the results. For the waveform cross-correlation between the two events, time windows centred at the measured arrival times were

interpolated at a sampling rate of 1000 Hz, and the maximum cross-correlation coefficient (maxCC) of 3-s time windows were measured by allowing up to ± 1.5 s time-shifts (e.g. Hauksson & Shearer 2005). All the seismograms were bandpass-filtered from 1 to 10 Hz before the cross-correlation, and the traveltimes differences between the two waveforms were used only if the maxCC was above 0.85. To allow the bootstrapping to test the relocation uncertainties, the events were relocated by resampling the differential travel times for each event pair. The mean of the standard deviations of the 20 trials corresponds to 37 m horizontally and 54 m vertically, respectively.

3.2 Absolute location

During the study period, 2931 earthquake candidates were automatically detected, and 2848 earthquakes within 80 km of the epicentre of E2 were selected through the manual inspection of waveforms (Fig. 2). Only 148 events (5.2 per cent) occurred before the onset of E1. These events were mainly observed in offshore regions or along several local fault structures (Fig. 2a). However, only two events were located within 10 km of the epicentre of E2 during this period, and the background seismicity near the aftershock region is therefore considered insignificant. After the onset of E1, the number of earthquakes located outside the 10 km radius from the E2 epicentre was 146 (5.1 per cent), and their locations were similar to those that occurred before E1. However, some regions experienced spatial changes in seismic activities following the occurrence of E1. For example, the earthquakes at the location where the Ulsan and Dongrae Faults intersect shifted 5 km to the south (see the blue

circled area in Fig. 2a). The earthquakes near the Miryang Fault migrated to the north by a few kilometres (see the magenta circled area in Fig. 2a). These observations suggest that the seismicity changed due to the Gyeongju earthquakes, although it is hard to verify for how long these changes are maintained.

Starting from E1, 2552 events (89.6 per cent) occurred within 10 km from the epicentre of E2, and the distribution of the hypocentres showed a trend along the NNE–SSW direction (Fig. 2b). Although their epicentres are mainly located between the two surface fault traces of the Yangsan and Deokcheon Faults striking to the NNE–SSW or N–S direction (Kim *et al.* 2017c), the spatial distribution of the earthquakes does not exactly coincide with the surface geological features (Fig. 2b).

3.3 Double-Difference relocation

Including the three largest events, 2493 events were relocated within 10 km from the epicentre of E2 (Fig. 3a). This number is ~ 5 times greater than that of the relocated events of previous studies, which only used data from permanent station networks for a similar period (Son *et al.* 2017). This result illustrates the importance of aftershock monitoring networks for observations of microseismic events (Kim *et al.* 2016a; Kim *et al.* 2017a). In the map view, aftershocks are primarily aligned along N26° E, extending 5 km in the fault-parallel direction and 2 km in the fault-normal direction. The focal depths of the earthquakes range from 12 to 16 km (Figs 3c and d). Comparing the spatial pattern of the relocated hypocentres with that obtained from the single difference method, we can clearly observe the distinctive fault geometries that cannot be resolved in the initial distribution. In particular, it seems that the largest events (E1 and E2) occur independently on two distinct subparallel faults with an offset of 600–700 m, while E3 occurred on a conjugate fault plane with an ESE–WNW strike (Fig. 3a). For convenience, hereafter, we refer to the three fault planes overlapping with the locations of E1, E2 and E3 as F1, F2 and F3, respectively. The sizes and shapes of each fault plane are estimated from the hypocentre distributions.

The F1 plane strikes at N26° E and deepens towards the southeast direction with a dip angle of 65° in the depth range of 13.0–16.0 km; it is 3.0 km long and 3.1 km wide, comprising a square-like fault plane (Fig. 3c). Located to the east of F1, F2 has the same strike as F1, but the dip angle of the fault plane varies with the depth range and can be separated as: (1) F2a with a dip of 55° and a depth range of 11.5–13.5 km and (2) F2b with a dip of 69° and a depth range of 12.5–16.0 km (Figs 3c and d). E2 is located on F2b, whose dip angle is matched with that of one nodal plane of the E2 calculated moment tensor solution. The widths of F2a and F2b correspond to 2.4 and 3.7 km, respectively, while the lengths of F2a and F2b are the same at 5.5 km. The strike of F3 is set to N116° E, since the earthquakes near E3 are aligned perpendicularly to the strikes of F1 and F2. However, the number of earthquakes distributed over the streak is not enough to infer the dip angle. Therefore, we modelled F3 as a vertical fault plane based on the moment tensor inversion of E3 (Fig. 3a). Using the spatial distribution of the aftershocks for an hour from the onset of E3, the length and width of F3 were set to 1.0 and 0.7 km, respectively. The parameters of each fault plane are summarised in Table 1, and the schematic diagram is illustrated in Fig. 4.

E1 and E2 are located at the northeastern part of F1 and southwestern part of F2 compared with the spatial distribution of the

aftershocks (Figs 3c and d). The asymmetric aftershock distributions with respect to hypocentres may suggest that E1 and E2 ruptured towards the southwest and northeast, respectively (Mendoza & Hatzell 1988). This is consistent with the rupture directivity inferred from the finite fault slip models of E1 and E2 (Uchide & Song 2018).

4 AFTERSHOCK STATISTICS

4.1 Magnitude estimation

Choosing from among the various methods to estimate earthquake magnitude, we used the scaling relationship between magnitude differences and amplitude ratios. If two events have similar ray paths, focal mechanisms and source time histories, the magnitude difference (dM) between them can be expressed as:

$$dM = c \log_{10} \alpha, \quad (1)$$

where α is the amplitude ratio of one event to the other event, and c is a linear scaling parameter between the amplitude ratio and the magnitude difference (Shelly *et al.* 2016). In this study, the linear relationship and scaling parameter (c) of eq. (1) were investigated using aftershocks in the KMA catalogue, and the magnitudes of the aftershocks detected were relatively determined from linear scaling with the KMA catalogue events.

For the cross-correlation measurements applied in the relocation procedure, the amplitude ratios between two waveforms aligned by their phase arrival times were measured as the slope of the principal component obtained from the principal component analysis (PCA) for the data vectors (e.g. the amplitude relation between two aligned waveforms on a specific channel; see details in Fig. 2 of Shelly *et al.* 2016). The PCA sequentially finds principal components, which show the relationships among variables (Jolliffe 2011). Compared to measuring peak amplitude ratios, this method is known to give reliable amplitude ratios because it applies full waveforms, unlike other methods that use only the differences in peak amplitude values (Shelly *et al.* 2016). Fig. 5 illustrates that the logarithms of the amplitude ratios are approximately linearly proportional to the magnitude differences for the 165 events in the KMA catalogue that are also listed in our event catalogue. The c values estimated from the least squares method and PCA are not significantly different (0.62 and 0.69, respectively). Of the two methods, the c value is taken from the PCA, since it is a more appropriate approach for extracting patterns among variables without assigning dependent and independent variables (Jolliffe 2011).

For the whole set of aftershocks, we calculated the amplitude ratios between the target events and KMA catalogue events in the same manner for the estimation of the c value. Each measured amplitude ratio for a target event is translated to a relative magnitude by using eq. (1) and a c value of 0.69. To increase the reliability of the results, the magnitudes of the target events were estimated by averaging the magnitudes obtained from more than 10 measured amplitude ratios. Here, we define the estimated magnitudes as M_{rel} since eq. (1) can be valid for a limited range of magnitudes. From the procedure, the magnitudes of 2560 earthquakes were relatively estimated.

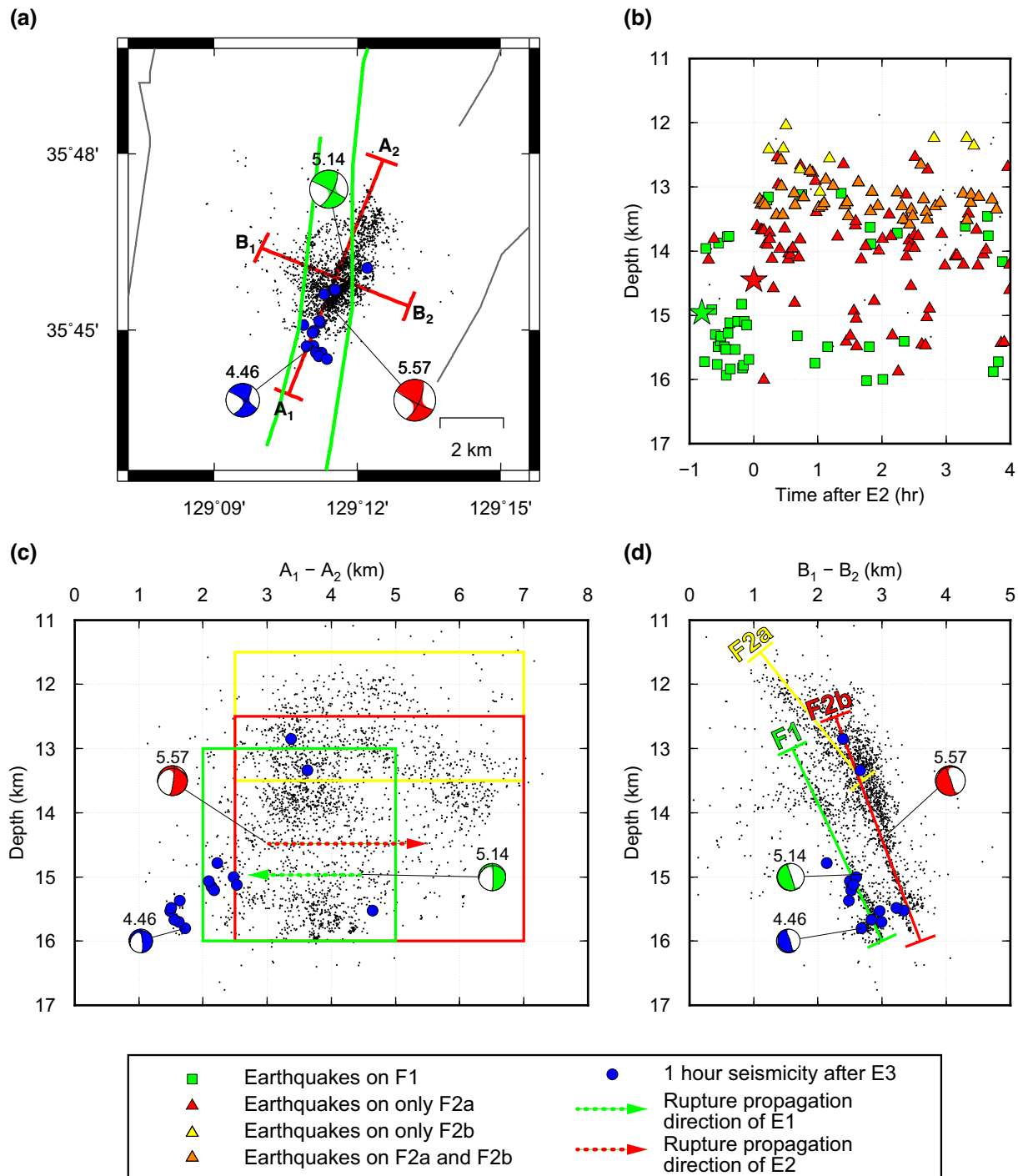


Figure 3. Distribution of the 2510 relocated hypocentres in the aftershock region. (a) Distribution of the epicentres of the Gyeongju earthquakes. (b) Five-hour seismicity at the early stage of aftershocks as a function of focal depth. Four different symbols are used for the events in four selected periods. (c–d) The depth distributions along A₁–A₂ (oriented N26° E) and B₁–B₂ (oriented N116° E). The three moment tensor solutions of E₁, E₂ and E₃ are distinguished as three different colours of compressional quadrants: green (E₁), red (E₂) and blue (E₃). The blue dots in (a), (c) and (d) represent one hour of seismic activities following E₃, and the estimated rupture propagation directions of E₁ and E₂ by Uchide & Song (2018) are denoted as green and red arrows, respectively. Fault geometries of F₁, F_{2a} and F_{2b} are illustrated as green, yellow and red lines, respectively. The other symbols match those in Fig. 1.

4.2 Spatial and temporal characteristics of aftershock activity

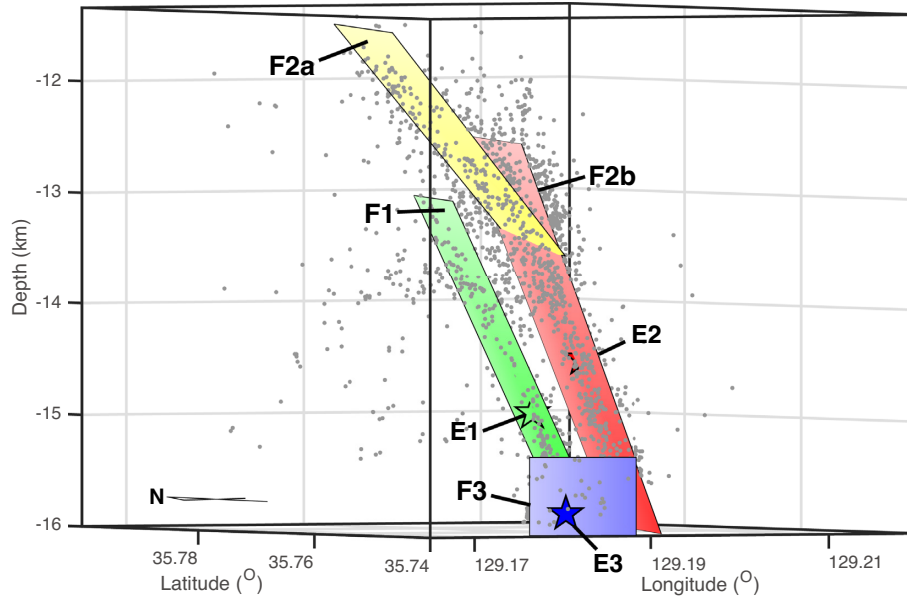
As characteristics for aftershock occurrences, the frequency–size distribution and the aftershock decay rate have been applied in many cases (Wiemer & Katsumata 1999; Aktar *et al.* 2004; Zhao &

Wu 2008; Enescu *et al.* 2011; De Gori *et al.* 2014; Abdelfattah *et al.* 2017; Ansari 2017). The former characteristic can be expressed in the following way:

$$\log_{10} N = a - bM, \quad (2)$$

Table 1. Geometric parameters of the three major fault planes.

Fault ID	Width (km)	Length (km)	Min depth (km)	Max depth (km)	Area (km ²)	Strike/dip (°)	Number of earthquakes
F1	3.1	3.0	13.0	16.0	9.3	26/65	507
F2a	2.4	5.5	11.5	13.5	13.2	26/55	541
F2b	3.7	5.5	12.5	16.0	20.4	26/69	1173
F3	0.7	1.0	15.3	16.0	0.7	116/NA	34

**Figure 4.** A 3-D schematic diagram to illustrate the spatial distribution of the aftershocks and the geometry of the four faults (F1, F2a, F2b and F3). Detailed information for each fault is summarised in Table 1.

where N is the cumulative number of earthquakes with magnitudes equal to or greater than M . The a -value and b -value, which are generally treated as constants, reflect the characteristics of earthquakes in a particular region and period. However, they can change with time or location. In particular, the b -value can be affected by various physical properties such as asperities, effective stress, material heterogeneity, crack density, thermal gradient and tectonic regimes (Wiemer & Katsumata 1999; Westerhaus *et al.* 2002; Schorlemmer *et al.* 2005; Goebel *et al.* 2012; Tormann *et al.* 2014; Raub *et al.* 2017).

The frequency of aftershocks generally decreases in inverse proportion to time, and the tendency can be expressed using Omori's formula:

$$R(t) = K(t + c)^{-p}, \quad (3)$$

where K , c and p are constants to be determined. In particular, the p -value that represents a measure of the decay rate of the seismic activities is known to vary from 0.6 to 1.8 (Wiemer & Katsumata 1999), and many factors influence the variation in p -value, including structural heterogeneity, stress and temperature in the crust (Utsu & Ogata 1995).

In this study, we reasoned that the minimum magnitude of completeness (M_c) that satisfies eq. (2) changes over time due to the expansion of the temporary observation network, affecting the estimation of b -values and p -values. Therefore, we first analysed the temporal variations in b for every set of 500 events in chronological order by allowing duplication of 400 events, considering the time-variant M_c (Figs 6a and b). We then estimated b -values and p -values for all aftershocks and for two event subsets on F1 and F2 for the

maximum value of M_c (Figs 6c and d). The b -value for each event set is evaluated from the maximum likelihood method by Aki (1965) with a magnitude bin size (ΔM) of 0.1, and the uncertainty of each estimated b -value is calculated by using the Shi & Bolt (1982) equation. The M_c is calculated from a modified goodness-of-fit method from Wiemer & Wyss (2000). After the calculation of the goodness-of-fit value for every M_c with a 0.1 interval, we find the minimum M_c (M_{cmin}) for which the goodness-of-fit value is greater than 0.9 and take the M_c that yields the maximum goodness-of-fit value in the range of $[M_{cmin}, M_{cmin} + 2\Delta M]$. The three constants and their standard deviations in eq. (3) for each event set with magnitudes greater than M_c are estimated from the maximum likelihood procedure of Ogata (1983).

The results of the time-variant M_c and b -values are presented in Figs 6(a) and (b). For the first 3 d, M_c decreases from 1.3 to ~ 1 and remains at ~ 1 for the subsequent period (Fig. 6a). The b -value, on the other hand, is 0.82 ± 0.04 at the initial stage and increases to 1.14 ± 0.06 during the three days after the onset of E1 (Fig. 6b). The b -values of the total data set and the events on F1 and F2 are approximately the same at 0.98 ± 0.03 , 0.99 ± 0.07 and 0.98 ± 0.04 , respectively, but the p -values of the three event sets are 1.03 ± 0.08 , 0.89 ± 0.03 and 1.13 ± 0.08 , respectively, which are slightly different from one another (Figs 6c and d). For each event set, the M_c for calculating the b -values and p -values is fixed to 1.3, which is the maximum value over time.

The initial 3 d of decreasing M_c correspond exactly to the period in which the temporary observation network was being expanded. The decrease in M_c during the early earthquake sequences may come from the high level of background noise. However, we ensured

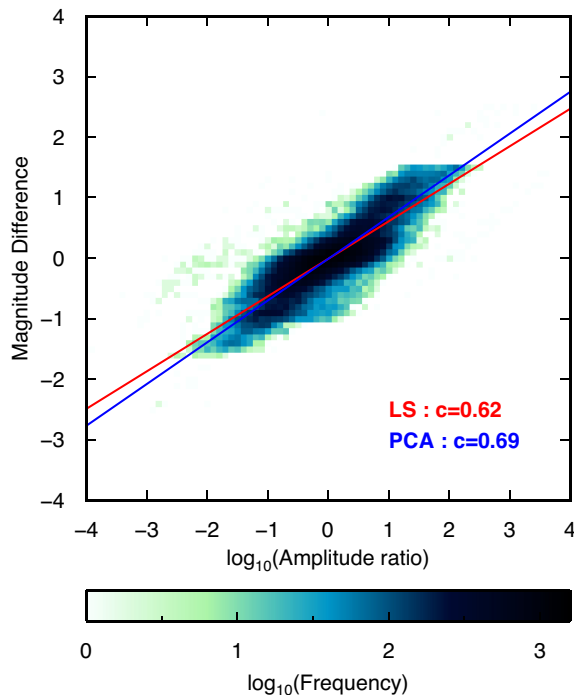


Figure 5. Determination of the scaling parameter c in eq. (1) by using KMA catalogue events. For an event pair, the logarithm of the amplitude ratio measured from waveform data and the magnitude differences between the two events correspond to the abscissa and ordinate of the graph. Two methods were tested for the estimation of the c value: the least squares method (red line; $c = 0.62$) and the principal component analysis method (blue line; $c = 0.69$).

that the temporal change in Mc does not appear in the results from the 959 earthquakes detected by using only the eight permanent stations.

The b -value temporarily increased from 0.82 to 1.14 during the initial three-day period in which the seismic observation network was being expanded. We tested and confirmed that the increasing trend still appears even if Mc is fixed to the highest value (i.e. 1.3) and confirmed that the choice between various Mc and fixed Mc does not affect the increase in b -value. The two event segments marked as solid red dots are offset by 3 d, and their b -value difference is estimated as 0.32 (Fig. 6b). To determine whether or not the difference between the two b -values is statistically significant, we applied Utsu's (1992) test, and the probability that there would be no difference in the b -value between the two sets of populations is estimated as 9×10^{-5} , confirming that the difference in the b -values of the two sets of data would be statistically significant.

The tendency for b -values to increase after the onset of an earthquake has been observed in other cases: the 2004 M_s 6.0 Parkfield earthquake (Shcherbakov *et al.* 2006) and the 1999 September 13 M_w 5.8 event between the Izmit epicentre and Lake Sapanca (Raub *et al.* 2017). Raub *et al.* (2017) estimated that the increase in b -values is related not only to the release of stress but also to the unclamping of faults. Hosono & Yoshida (2002) reported that the expected number of relatively large earthquakes is lacking in later earthquake sequences compared with that calculated from the modified Omori formula for an early time period, and this effect may result in the relatively small b -values at the initial stages.

The estimated b -values for all data sets, E1 and E2 are all close to 1 and consistent with the estimation of 1.04 for the KMA catalogue events (Hong *et al.* 2017). This b -value of 1 also corresponds to the commonly observed value in other earthquake sequences (Wu *et al.* 2015; Ansari 2017). The p -value of 1.03 for the entire data set is considerably lower than the 1.53 value of Hong *et al.* (2017), who also used the KMA catalogue events. The disparity can be attributed to the use of different fitting ranges in Omori's Law or the additional consideration of Mc for determination of the p -values.

5 MOMENT TENSOR SOLUTIONS AND FOCAL MECHANISMS

5.1 Method of analysis

In this study, the deviatoric moment tensor solutions were determined using the ISOLA software of Sokos & Zahradnik (2008) for 10 selected earthquakes with $M_L \geq 3$. After several trials were attempted for the appropriate stations and filtering ranges, the moment tensor solutions of the 10 selected earthquakes were determined using the waveforms recorded at four or five stations, and two different frequency ranges of 0.05–0.1 Hz were used for the three largest events, while 0.08–0.16 Hz were used for the rest. The optimal focal depths were determined from moment tensor inversion by testing different depth ranges with a 1-km bin. The same regional one-dimensional velocity model used in the location procedure (e.g. Kim *et al.* 2011) was used to construct Green's functions as well.

For 519 aftershocks with more than 20 P -wave arrival times, the P -wave polarities at each station were manually measured, and we applied the FOCMEC software of Snoke (2003) to calculate their focal mechanisms. The focal mechanism analysis was performed only if an earthquake had at least 10 polarity measurements. We sorted out the candidate focal mechanisms with minimum measurement errors for each event and excluded events from the analysis if candidate solutions contained polarity errors larger than three. Among the possible solutions for each event, we selected one optimal solution, of which the sum of the distances from its P -, T - and B -axes to all other solutions on the focal sphere is minimised. All solutions, including the selected optimal solution, are visually inspected to confirm similarity in the mechanisms. We obtained 263 reliable focal mechanisms in this procedure.

5.2 Results

The detailed moment tensor inversion results of the 10 selected events are given in Fig. 7 and Table 2. Although some earthquakes have a considerable amount of compensated linear vector dipole components (~ 20 per cent), double-couple components are generally dominant. All inverted moment tensor solutions are classified as strike-slip events, of which one nodal plane is parallel to F1 and F2, which is consistent with previous research studies (Son *et al.* 2017; Kim *et al.* 2017a). Assuming that the fault rupture of each earthquake propagates on F1 or F2, the true fault plane has an NNE–SSW strike direction with right-lateral movement.

We classified the 263 focal mechanisms estimated by the P -wave first motions according to the ternary diagram of Frohlich (1992). The number of earthquakes that correspond to strike-slip events and thrust events were 174 (66 per cent) and 54 (21 per cent),

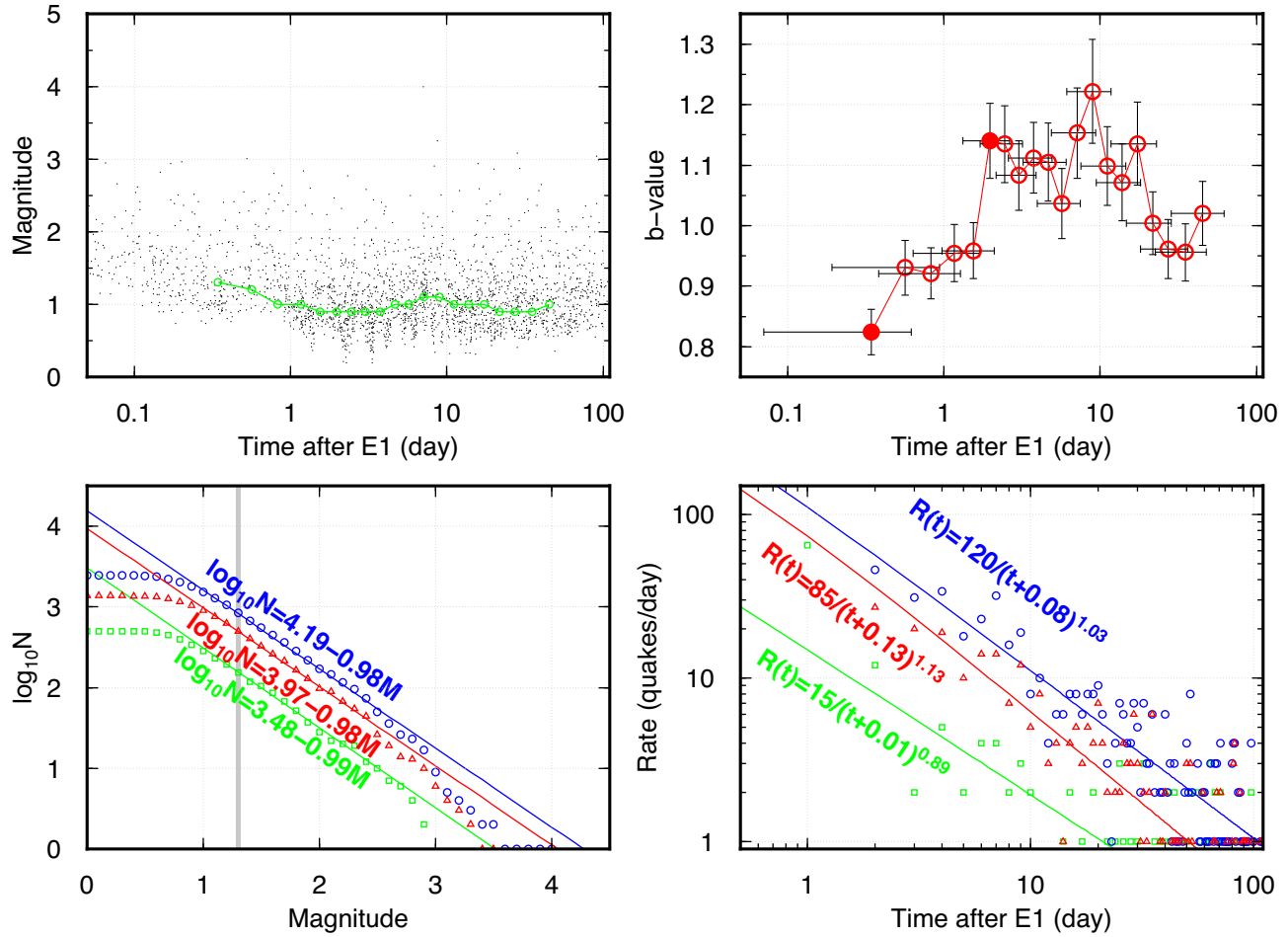


Figure 6. (a) Event magnitudes as a function of time. The temporal variation in M_c is represented as a green line. (b) The b -value variation is a function of time. The horizontal and vertical error bars indicate one standard deviation of event origin times and b -values, respectively. The b -value difference between two event sets denoted as solid red dots was tested by Utsu's test (see Section 4.2). (c) The frequency–magnitude distribution of the three event clusters: all events (blue dots), F1 (green dots) and F2 (red dots). A grey line represents the M_c used for estimation of b -values. (d) The occurrence rate of the three event clusters: all events (blue dots), F1 (green dots) and F2 (red dots). The three lines with different colours in (c) and (d) represent the obtained G-R law and modified Omori's Law, respectively.

respectively. The remaining events were classified as odd faulting types, while no normal faulting events were observed. From the spatial distribution of the strike-slip events and thrust events, which account for 87 per cent of the calculated focal mechanisms, we can observe that both types of focal mechanisms occur on both F1 and F2 (Fig. 8).

The trend and plunge of the P -axis of the strike-slip events are $75^\circ \pm 11^\circ$ and $10^\circ \pm 7^\circ$, respectively, and those of the thrust events are $77^\circ \pm 20^\circ$ and $14^\circ \pm 10^\circ$, respectively, indicating that the trend of the maximum principal stress axis is homogeneous at 70 – 80° . However, despite the coexistence of the two faulting types on both F1 and F2, the detailed spatial distributions of the strike-slip and thrust events are quite different from each other, implying that the other principal stresses are locally heterogeneous.

Reliability of the determined faulting types is verified by visually comparing the observed and expected P -wave amplitudes. For example, P -wave amplitudes recorded near the epicentres of strike-slip events should be weak, but they should be positive and large for thrust events. In order to cross-check the reliability of the inverted fault parameters calculated by the methods implemented in the FOCMEC and ISOLA software, the focal mechanisms of the

four earthquakes inverted from both methods were compared, and no significant differences were observed.

6 STRESS INVERSION

As mentioned in the previous section, the inverted focal mechanisms of the 263 events are mainly divided into strike-slip and thrust events under the homogeneous P -axis, and their spatial distributions are different from each other. One key observation is that thrust earthquakes rarely occur at depths deeper than ~ 15 km, whereas strike-slip earthquakes occur at greater depths (e.g. the sub-region of C3 in Figs 8b, c, e and f). Another important observation is that thrust events are predominantly scattered in areas with depths shallower than 13.5 km and horizontal distances greater than 5 km on the A1–A2 profile (e.g. the subregions of C4 in Figs 8b and e). The spatial heterogeneity of the fault types is indicative of the spatial heterogeneities observed in the tectonic stress field.

To examine the heterogeneity in the stress field of the after-shock region, the study area is divided into five subregions in which the spatial distribution of the strike-slip and thrust events

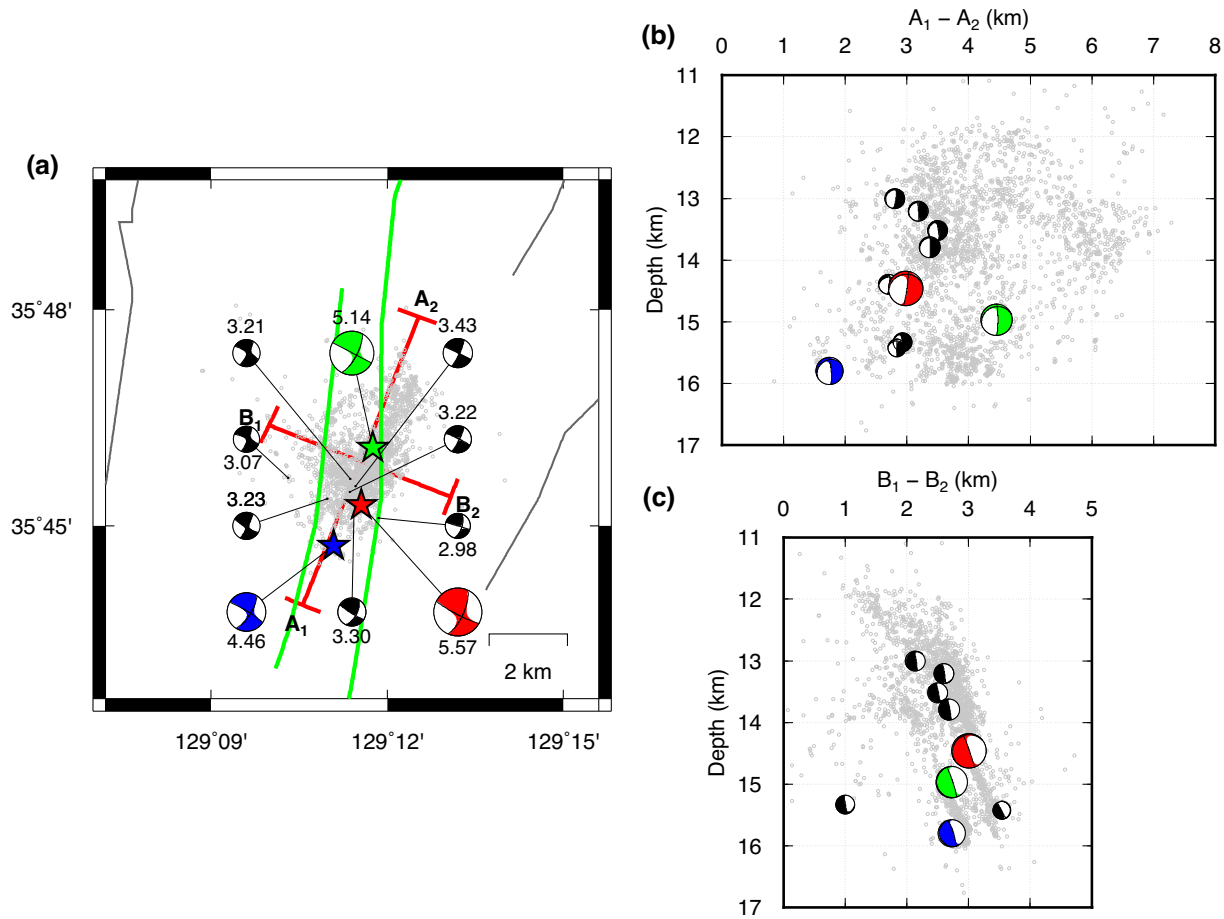


Figure 7. The spatial distribution of the 10 selected events with their deviatoric moment tensors. Each number above the moment tensor in (a) represents the moment magnitude of the event. The compressive quadrants of the three largest events in (b) and (c) are coloured in green (E1), red (E2) and blue (E3). All the relocated hypocentres are denoted as grey dots on the map in (a) and cross-sections in (b) and (c). The other symbols match those in Fig. 1.

Table 2. Source parameters of the ten earthquakes used in the moment tensor analysis.

Event ID	Event origin time (UTC) (yy/mm/dd, hh:mm:ss.ss)	Latitude (° N)	Longitude (° E)	Depth (DD; MTI, km)†	Magnitude (Mw)	Strike (°)‡	Dip (°)‡	Rake (°)‡	Double-couple component (%)	Maximum correlation*
155 (E1)	16/09/12, 10:44:33.04	35.768	129.196	15.0; 14;	5.14	27/297	71/89	-179/-18	82	0.98
191 (E2)	16/09/12, 11:32:54.55	35.755	129.193	14.5; 12	5.57	24/117	70/82	171/19	75	0.98
331	16/09/12, 14:18:28.55	35.761	129.172	15.3; 14	3.07	24/292	80/80	-170/-9	78	0.62
354	16/09/12, 14:52:31.06	35.761	129.190	13.5; 11	3.21	30/298	79/81	-171/-10	79	0.75
561	16/09/12, 23:24:48.34	35.756	129.183	13.0; 11	3.23	28/119	80/82	171/9	87	0.73
1631 (E3)	16/09/19, 11:33:58.81	35.745	129.185	15.8; 14	4.46	32/301; 30/120	72/85; 70/90	-174/-17; 180/20	82	0.98
1761	16/09/21, 2:53:55.13	35.759	129.191	13.8; 12	3.43	25/295; 30/120	79/89; 85/81	-179/-10; 171/5	97	0.91
2167	16/10/02, 11:53:07.96	35.752	129.198	15.4; 15	2.98	17/107; 10/110	62/89; 53/77	179/27; 164/38	91	0.62
2314	16/10/10, 13:59:10.61	35.753	129.191	14.4; 15	3.30	27/121; 36/133	62/83; 64/75	172/27; 164/27	97	0.79
2884	16/12/12, 08:53:18.14	35.758	129.189	13.2; 11	3.22	26/295	81/84	-174/-8	95	0.77

*Optimal focal depth of each event is one that maximizes cross-correlation coefficient between synthetic and observed waveforms.
†The depth of each event is calculated from both the Double-Difference (DD) relocation and the moment tensor inversion (MTI).
‡If we obtain the focal mechanism of an event using the first *P*-wave motions, we ordinarily describe the fault parameters obtained from the waveform inversion and first *P*-wave motions.

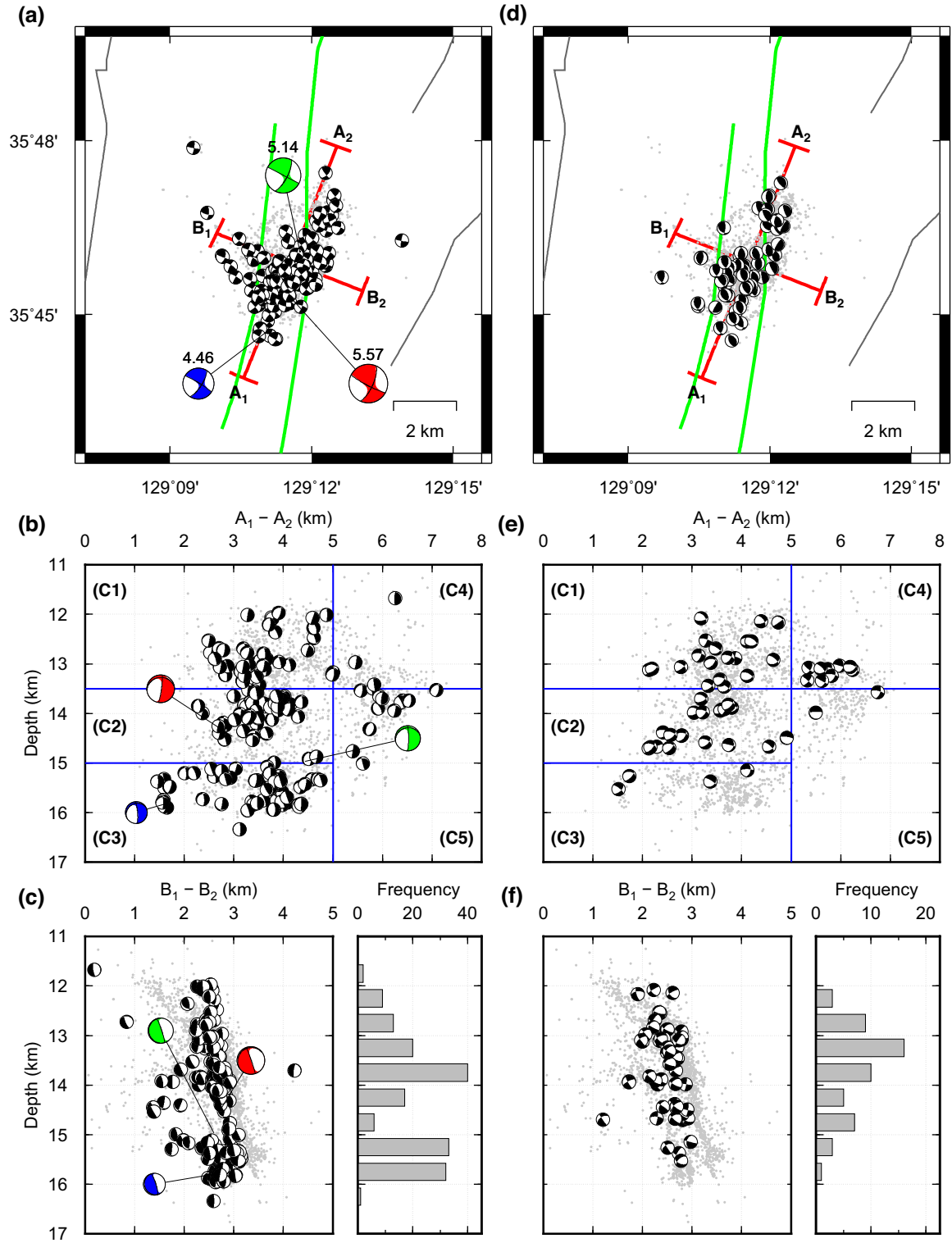


Figure 8. The hypocentre distribution of the 174 strike-slip events (a–c) and 54 thrust events (d–f) classified by Frohlich (1992) and the histograms for the number of strike-slip and thrust events as a function of focal depth (right panels of c and f). The moment tensor solutions of E1, E2 and E3 are illustrated in (a–c) with green, red and blue compressional quadrants. The subregions of C1–C5 in (b) and (e) divided by blue lines represent the domains for the stress inversion (Fig. 9). The other symbols match those in Fig. 1.

varies, and the stress inversion was performed for each subregion (Fig. 9). The inversion was applied via the MSATSI software, which was redesigned from the conventional SATSI algorithm for use in the MATLAB environment (Hardebeck & Michael 2006;

Martínez-Garzón *et al.* 2014). No regularization for the spatial difference of the stress field is applied, and one fault plane from two conjugated planes is randomly selected by considering the fault plane ambiguity. Detailed inversion parameters, such as the number

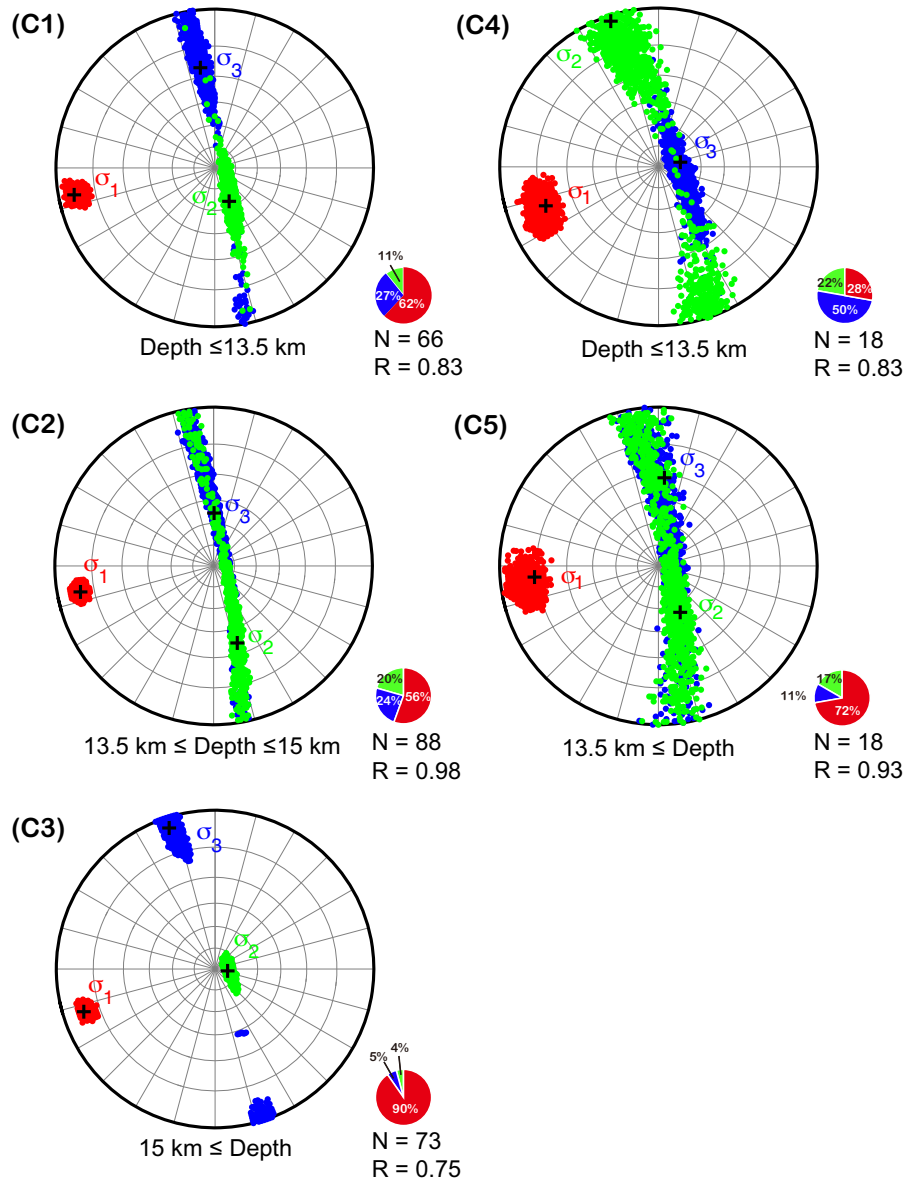


Figure 9. Stress inversion results for the events in the five different blocks (C1–C5). First, the study area is divided into the left section (C1, C2 and C3) and the right section (C4 and C5) at the 5-km point on the A1–A2 profile. Then, each section is split into two or three subsections with different depth ranges. For each subplot, the depth ranges, relative stress magnitude (R), and number of focal mechanisms used (N) are shown below the inversion results. Each subplot is illustrated with a pie-chart representing the relative portions of strike-slip events (red), thrust events (blue) and other types of events (green). The three principal stress components ($\sigma_1 > \sigma_2 > \sigma_3$) are represented with 1000 bootstrapping results. The maximum principal stress (σ_1) is well resolved with low uncertainty for all the subsections. Except for C3, the other principal stress components are not constrained due to the mixed population of strike-slip events and thrust events.

of fault planes used and the direction of each principal axis, are presented in Fig. 9.

Trends and plunges of the maximum stress components (σ_1) in all subregions are estimated as $\sim 260^\circ$ N and $\sim 10^\circ$, respectively, which suggests that the maximum horizontal stress (σ_{Hmax}) is homogeneous in the study area. However, the intermediate stress field (σ_2) and the minimum stress field (σ_3) are not uniform in the five subregions. In the depth range less than 13.5 km, σ_2 in C1 and C4 corresponds to the minimum horizontal stress (σ_{hmin}) and the lithostatic stress (σ_v), respectively. At intermediate depths (13.5–15 km), the amplitudes of σ_2 and σ_3 are so close to each other that they cannot be well constrained (Fig. 9). For C3 at depths <15 km, all the principal stress orientations are well constrained

due to the dominance of strike-slip events. The R values, defined as $(\sigma_1 - \sigma_2)/(\sigma_1 - \sigma_3)$, are equal to or greater than 0.75 throughout all subregions, suggesting that the aftershock region is in the transpressional regime (Bohnhoff *et al.* 2006).

In C3, where σ_2 and σ_3 are clearly distinguished as the vertical stress and minimum horizontal stresses, the principal stresses normalised by vertical stress can be derived from the Coulomb Friction Law and the R value, with the assumption that excessive differential stresses would be released by slip along optimally oriented fault planes (Jaeger *et al.* 2009; Soh *et al.* 2018). Based on the frictional coefficient (μ) of 0.85 and the hydrostatic pore pressure, the relative minimum horizontal stresses (σ_{hmin}/σ_v) and the relative maximum

horizontal stresses ($\sigma_{\text{Hmax}}/\sigma_v$) correspond to 0.70 and 1.94, respectively, which are consistent with the results of Soh *et al.* (2018). If μ varies from 0.6 to 1 following Byerlee's Law (Byerlee 1978), $\sigma_{\text{Hmin}}/\sigma_v$ and $\sigma_{\text{Hmax}}/\sigma_v$ have a range of 0.66–0.79 and 1.67–2.07, respectively. If we assume a unit weight of granitic rocks for the continental crusts (26.5 kNm⁻³, Soh *et al.* 2018), the values of σ_{Hmax} , σ_v and σ_{Hmin} at a depth of ~ 16 km are estimated as 823, 424 and 297 MPa, respectively.

7 STRESS TRANSFER ANALYSIS

The 50-min gap between the origin times of the E1 and E2 events and the 600–700 m offset of the two faults (F1 and F2) may indicate the static stress interaction in a multifault system. In other words, the perturbed stress field caused by the seismic activity on F1 may have affected the spatial and temporal distribution of earthquakes on F2, and vice versa. One of the favourable approaches with regard to the triggering of earthquake aftershocks is the Coulomb hypothesis, which explains the increased (or decreased) seismicity with regional static stress changes. For a specific receiver fault, the relationships among the Coulomb stress change ($\Delta\sigma_f$), shear stress change ($\Delta\tau$), normal stress change ($\Delta\sigma$) and pore pressure change (ΔP) on this fault are given as:

$$\Delta\sigma_f = \Delta\tau + \mu(\Delta\sigma + \Delta P), \quad (4)$$

where μ is the coefficient of internal friction, and unclamping is defined as positive for the normal stress (Lay & Wallace 1995). If we use the apparent frictional coefficient μ' instead of μ , which involves both the effects of pore pressure changes and normal stress changes, then eq. (4) can be rewritten as (Reasenber & Simpson 1992; King *et al.* 1994):

$$\Delta\sigma_f = \Delta\tau + \mu'\Delta\sigma. \quad (5)$$

We applied two approaches for the Coulomb stress calculations via the Coulomb 3.3 software (Lin & Stein 2004; Toda *et al.* 2005). First, the Coulomb stress changes imparted by both E1 and E2 were analysed for optimally oriented strike-slip faults to resolve the temporal variation of the off-fault seismicity. The epicentres of detected events determined by the single difference method in Fig. 2 were compared with the Coulomb stress changes on the optimally oriented receiver fault for the maximum stress field in the N75° E direction, with a strength of 65 bars (Hong *et al.* 2017). We then calculated the Coulomb stress changes on F1, F2 and F3 from the E1 and (or) E2 slip models to check whether the static stress change of each fault plane correlates with off-fault seismicity. Following the scheme of Hong *et al.* (2017), the apparent frictional coefficient μ' , Young's modulus and Poisson's ratio were set to 0.4, 80 GPa and 0.25, respectively. The finite rupture models of E1 and E2 from Uchide & Song (2018) were used to configure the slip amounts on the faults.

Fig. 10 illustrates the Coulomb stress changes on optimally oriented faults at a depth of 14 km generated by both E1 and E2 with the epicentres of all located earthquakes. In the region far from F1 and F2 (i.e. the area outside of the black box in Fig. 10), the seismicity increases within the area of positive Coulomb stress changes and decreases within the negative lobes. More specifically, the effects of the Coulomb stress changes were inversely proportional to the epicentral distances up to ~ 50 km (see the upper right-hand panel of Fig. 10).

The calculated Coulomb stress change on F2b for the fault model of E1 gives a negative value at the loci of E2. However, an elliptical

patch with positive Coulomb stress changes was observed near E2, not more than 500 m away (Fig. 11a). If the uncertainties of the finite slip model and relocated hypocentre are taken into account, the Coulomb stress changes by E1 may have advanced the occurrence of E2, although dynamic stress changes, fault geometries and the regional stress state can affect the result (Gomberg *et al.* 2003). The fault model of E2 yields positive Coulomb stress changes on an inverted T-shaped area (Fig. 11b). The seismic activity on F1 for 5 hours after E2 overlaps with the area, implying that the Coulomb stress change caused by the occurrence of E2 may also have affected the seismicity on F1. Slips from both finite fault models of E1 and E2 result in positive Coulomb stress changes on the sinistral slip of F3 (~ 7 bar), which may indicate that the Coulomb stress changes imparted by the two largest events trigger the sinistral slip of E3 on a conjugate fault striking to the ESE–WNW direction.

8 DISCUSSION

8.1 Fault system complexity

The detailed spatial distribution of the Gyeongju earthquakes represents the occurrence of E1 and E2 on two parallel fault planes of F1 and F2, with an offset of 600–700 m. Complex fault systems with two or more parallel faults can also be found in other regions (Durá-Gómez & Talwani 2009; Rabak *et al.* 2010; Yano & Matsubara 2017). Yano & Matsubara (2017) reported that part of the 2016 Kumamoto earthquake sequence was aligned on two vertical fault planes in the northeastern area of Mt Aso with two moderate-sized aftershocks ($M \geq 5$) located on either side of the fault plane. This is consistent with our results that major events in a sequence separately occurred on visually identified faults.

The third largest event (E3), located at the southwestern tip of the aftershock region, and a streak of earthquakes following E3 are aligned on F3, which is perpendicular to F1 and F2 (Fig. 3a). Conjugate fault systems can be found in many previous studies (The 2012 Sumatra earthquake, Meng *et al.* 2012; The 2000 Wharton Basin earthquake, Robinson *et al.* 2001; The 2000 Western Tottori earthquake, Fukuyama *et al.* 2003). In particular, the 2000 Western Tottori earthquake has characteristics similar to the Gyeongju earthquake in that relatively small conjugate faults ruptured at the tip of the main faults.

The dip of F2 estimated from relocated earthquakes varies at a depth of ~ 13.5 km (Fig. 3d). Therefore, we suggest that the fault plane is bent or that two distinct faults having different dips are crossing at the region. To check that an inaccurate velocity model affects the fault structure, various velocity models were tested and significant changes were not observed.

8.2 Interactions between complex faults

The first couple of hours of spatio-temporal variations in seismicity on F1 and F2 are very characteristic. In the period between E1 and E2, most earthquakes are confined on F1 at a depth range of 15–16 km. Seismic activities on F1 abruptly diminished after the occurrence of E2 for at least four hours (Fig. 3b). Instead, most of the earthquakes following E2 are located at depths shallower than 14 km. This is in contrast to the deep seismic activity on F1 before E2. The decreased seismicity on F1 starting from the occurrence of E2 cannot be fully explained by static stress changes because the Coulomb stress changes on F1 imparted by the finite slip model of E2 are positive in some areas (Fig. 11b). Therefore, other factors

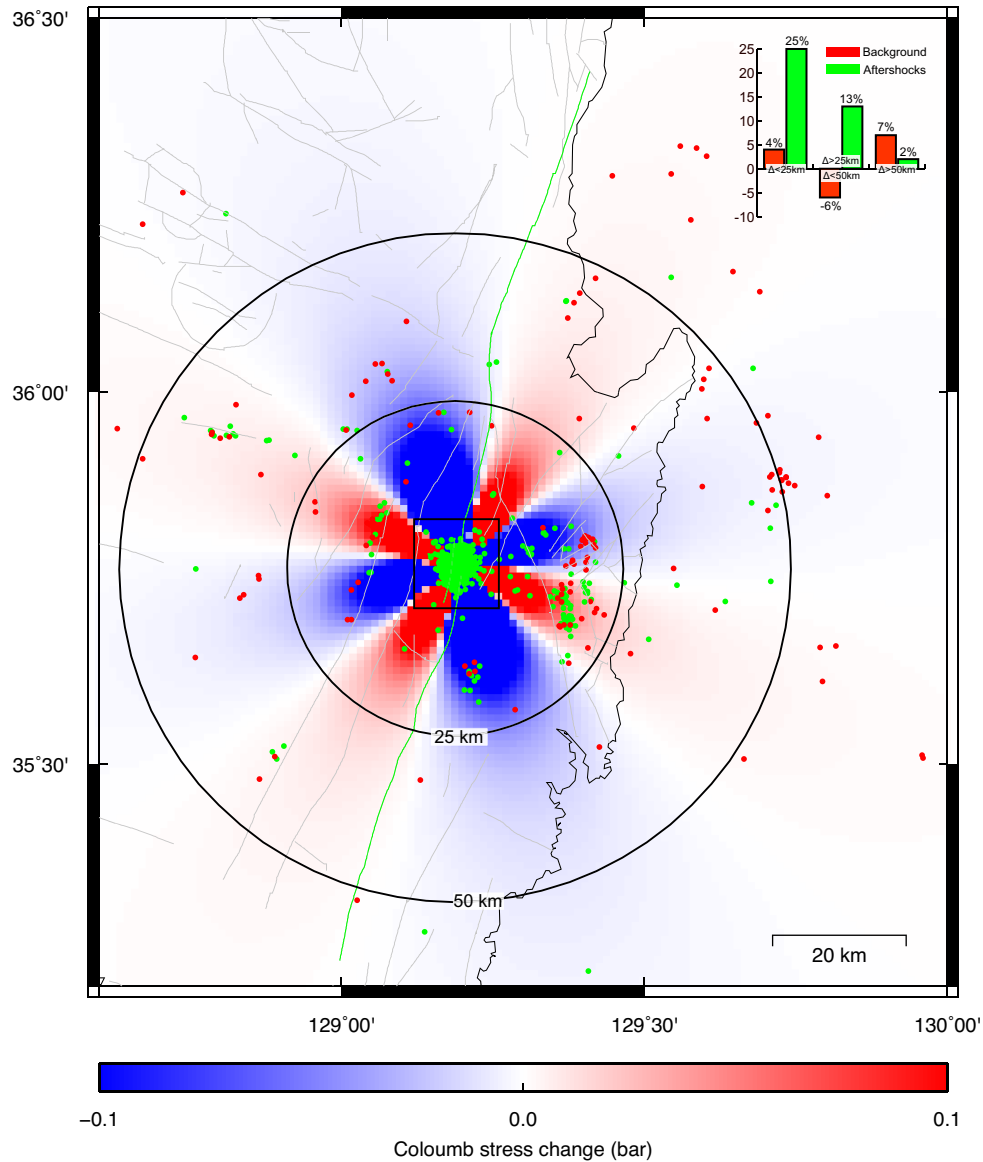


Figure 10. Coulomb stress changes on optimally oriented receiver faults at a depth of 14 km. Each sub-fault element is assumed to have an area of $1 \times 1 \text{ km}^2$. The seismicity values before and after the onset of E1 illustrated in Fig. 3(a) are shown with red and green dots, respectively. The off-fault seismic activities are regarded as the earthquakes that occur outside the black box. For each epicentral distance bin, the percentage difference between the off-fault earthquake densities of the areas with increased Coulomb stress changes and those with decreased Coulomb stress changes is illustrated in the inset histogram. The other symbols match those in Fig. 1.

such as irregular fault geometry, heterogeneous elastic modulus and complex stress states are required to explain it.

8.3 A possible microscale heterogeneity in the complex fault system

The b -values for F1 and F2 are almost unity, but the p -value for F1 is estimated to be significantly less than that of F2. The difference in p -values may result from the decreased seismicity of F1 after the occurrence of E2. To check the effect of initial earthquake sequences, the p -value for F1 was re-estimated after removing the earthquakes before E2. We confirmed that it remains at 0.96 ± 0.04 , which is still less than those for all data sets and events on F2. Therefore, it is reasonable that the decay rate of the seismicity on F1 is generally slower than that on F2. Still, many factors can

be attributed to the spatial changes in the p -values: stress, fault heterogeneity and crustal heat flow (Wiemer & Katsumata 1999; Enescu *et al.* 2011), requiring further analysis on this parameter in order to pinpoint the exact cause.

The maximum M_{rel} of the reverse fault earthquakes determined by focal mechanism inversion corresponds to 2.46. None of the fault types calculated from the moment tensor inversion has a thrust regime. Indeed, from the hypocentre distribution, no characteristic structure is identified along the NNE–SSW direction, the strike direction of the reverse faults. Therefore, the reverse fault events occur on smaller fault planes than those of the strike-slip events, and microcracks that cannot be identified by the hypocentre distribution may develop throughout the study area, generating the thrust events that occur in response to the heterogeneous stress field at each location.

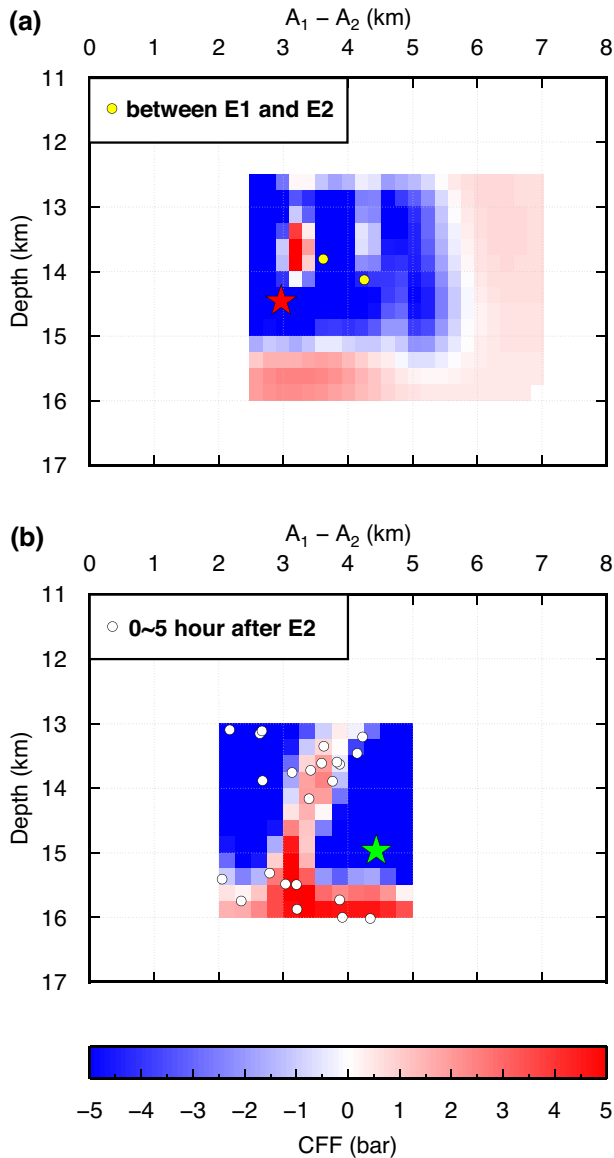


Figure 11. Coulomb stress changes imparted by the finite slip models of Uchide & Song (2018) on the subfault elements of other faults. (a) Coulomb stress changes on F2b caused by the finite slip model for E1. The seismic activities on F2 between the onsets of E1 and E2 are denoted as yellow dots. (b) Coulomb stress changes on F1 caused by the finite slip model for E2. Five hours of seismicity following E2 are shown as white dots. The green and red stars correspond to the locations of E1 and E2, respectively.

8.4 Model Implication

Background seismicity around the study area is concentrated along mapped faults, which indicates that earthquakes occurred on pre-existing faults where local stress had accumulated, rather than at newly formed faults (Fig. 2a; Lee & Jin 1991; Han *et al.* 2017; Kim *et al.* 2017b). The Gyeongju earthquakes ruptured beneath the Yangsan fault with a rupture length of 170–200 km and a horizontal offset of ~30 km (Fig. 2a, Kyung 2003; Kim *et al.* 2017b), but the general trend identified from the aftershocks is rotated clockwise by 15° from two mapped faults near the epicentres. Kim *et al.* (2017a) interpreted the angular difference as Riedel shears in a strike-slip duplex. However, we additionally identified F3 and thrust faults striking in different directions from the general

trends. Therefore, a more complicated structure than the simple Riedel shears is needed to explain minor faults. The hypothesis proposed by Uchide & Song (2018) suggested that the fault rupture models for E1 and E2 occurred in a fault jog of extensional oversteps and the pull-apart stress between them would produce normal faults in the aftershock area. However, we did not observe normal faulting events; we suspect that the faulting types of the Gyeongju aftershocks are more likely to be affected by local stress fields and pre-existing faults, rather than by the directivity of rupture propagations.

9 CONCLUSIONS

In this study, the source parameters of the Gyeongju earthquakes from 3 yr of seismicity data near the aftershock zone were analysed using data from a temporary seismic network as well as two permanent seismic networks. For the three largest earthquakes with $M_L > 4$, distinct fault planes at a depth of 12–16 km were identified. The two largest events (E1 and E2) occurred on two subparallel faults (F1 and F2) striking in the NNE–SSW direction, whereas the third largest event (E3) occurred on a vertical fault plane (F3) perpendicular to F1 and F2. The focal mechanisms estimated from the first motions of the P -waves are composed of strike-slip events, thrust events and intermediate types of events, which are not matched with an extensional fault jog and require modifications in the duplex strike-slip model. The strike-slip events are in accordance with the inverted moment tensors of the 10 selected events. The difference in the spatial distribution between the strike-slip events and thrust events indicates the heterogeneity between the minimum horizontal stress and lithostatic stress. In particular, reverse fault events are hardly observed deeper than 15 km, implying that the minimum horizontal stress is no longer greater than the overburden pressure below a depth of 15 km.

From the magnitudes of the earthquakes estimated by scaling the amplitude ratios and the magnitude differences, the temporal variations in the b -values and M_c were analysed over time. The b -values increased over the initial three days and did not vary significantly afterward. If the b -values are assumed to be a stress-metre indicator, the increase in b -values over time seems to reflect the stress releasing process. The b -values for both fault planes of F1 and F2 were close to 1, whereas the p -value for F1 is smaller than those for all the data and events on F2. The Coulomb stress changes caused by the two largest events are correlated with the spatial change of the seismic activities outside the aftershock region. It is possible that the occurrence of E2 is facilitated by the Coulomb stress changes imparted by E1 and that the Coulomb stress changes caused by E2 affect the seismicity of F1, and vice versa. However, a sudden reduction in the seismic activity on F1 following the onset of E2 could not be explained by static stress changes, indicating that complex fault properties are required to resolve it. The positive Coulomb stress changes for the sinistral slip of F3 generated by E1 and E2 may promote the occurrence of E3 at the southeast tip of the aftershocks. We suggest that our observations, such as the complicated spatio-temporal distribution of seismicity, heterogeneous stress field, and the p -value difference between the two parallel faults partially represents the complex fault properties of the Gyeongju earthquakes. More detailed models for fault geometry, local stress conditions and heterogeneous rock materials are required to fully understand the fault reactivation process of the complex fault system in the intraplate region.

ACKNOWLEDGEMENTS

We would like to thank the Korea Meteorological Administration (KMA) and Korea Institute of Geosciences and Mineral Resources (KIGAM) for sharing continuous waveform data for this study. Hobin Lim, Takahiko Uchide, Seok Goo Song, Miao Zhang, Chang-Soo Cho and two anonymous reviewers provided careful comments and suggestions which improved the manuscript. We are grateful not only to all the landowners and organizations that allowed us to install and operate temporary seismic stations on their properties but also to the graduate students in the Gyeongju earthquake research group for maintaining the temporary seismic network. Source parameters of the earthquakes analysed in this study is available at <https://github.com/Jeong-Ung/GJ>. This work was supported by the Nuclear Safety Research Program through the Korea Foundation of Nuclear Safety (KoFONS) using the financial resources granted by the Nuclear Safety and Security Commission (NSSC) of the Republic of Korea (No. 1705010).

REFERENCES

- Abdelfattah, A.K., Mogren, S. & Mukhopadhyay, M., 2017. Mapping b -value for 2009 Harrat Lunayyir earthquake swarm, western Saudi Arabia and Coulomb stress for its mainshock, *J. Volc. Geotherm. Res.*, **330**, 14–23.
- Adams, J., Wetmiller, R.J., Hasegawa, H.S. & Drysdale, J., 1991. The first surface faulting from a historical intraplate earthquake in North America, *Nature*, **352**, 617–619.
- Aki, K., 1965. Maximum likelihood estimate of b in the formula $\log N = a - bM$ and its confidence limits, *Bull. Earthq. Res. Inst.*, **43**, 237–239.
- Aktar, M. et al. 2004. Spatial variation of aftershock activity across the rupture zone of the 17 August 1999 Izmit earthquake, Turkey, *Tectonophysics*, **391**, 325–334.
- Ansari, S., 2017. Aftershocks properties of the 2013 Shonbe Mw 6.3 earthquake, central Zagros, Iran, *J. Asian Earth Sci.*, **147**, 17–27.
- Assumpção, M., Schimmel, M., Escalante, C., Barbosa, J.R., Rocha, M. & Barros, L.V., 2004. Intraplate seismicity in SE Brazil: stress concentration in lithospheric thin spots, *Geophys. J. Int.*, **159**, 390–399.
- Bianchi, M.B. et al. 2018. The Brazilian Seismographic Network (RSBR): improving seismic monitoring in Brazil, *Seismol. Res. Lett.*, **89**, 452–457.
- Bodin, P. & Horton, S., 2004. Source parameters and tectonic implications of aftershocks of the Mw 7.6 Bhuj earthquake of 26 January 2001, *Bull. seism. Soc. Am.*, **94**, 818–827.
- Bohnhoff, M., Gresser, H. & Dresen, G., 2006. Strain partitioning and stress rotation at the North Anatolian fault zone from aftershock focal mechanisms of the 1999 Izmit Mw = 7.4 earthquake, *Geophys. J. Int.*, **166**, 373–385.
- Byerlee, J., 1978. Friction of rocks, *Pure appl. Geophys.*, **116**, 615–626.
- Chang, K.H., 1977. Late Mesozoic stratigraphy, sedimentation, and tectonics of southeastern Korea, *J. Geol. Soc. Korea*, **13**, 76–90 (in Korean).
- Chen, Y., Tsoi, K.L., Chen, F., Gao, Z.H., Zou, Q.J. & Chen, Z.L., 1988. *The Great Tangshan Earthquake of 1976: An Anatomy of Disaster*. p. 153, Pergamon Press, New York.
- De Gori, P., Akinci, A., Pio Lucente, F. & Kılıç, T., 2014. Spatial and temporal variations of aftershock activity of the 23 October 2011 Mw 7.1 Van, Turkey, earthquake, *Bull. seism. Soc. Am.*, **104**, 913–930.
- Durá-Gómez, I. & Talwani, P., 2009. Finding faults in the Charleston area, South Carolina: 1. Seismological data, *Seismol. Res. Lett.*, **80**, 883–900.
- Enescu, B., Enescu, D. & Ito, K., 2011. Values of b and p : their variations and relation to physical processes for earthquakes in Japan and Romania, *Rom. J. Phys.*, **56**, 590–608.
- Ferreira, J.M., Oliveira, T., Takeya, M.K. & Assumpção, M., 1998. Superposition of local and regional stresses in northeast Brazil: evidence from focal mechanisms around the Potiguar marginal basin, *Geophys. J. Int.*, **134**, 341–355.
- Frohlich, C., 1992. Triangle diagrams: ternary graphs to display similarity and diversity of earthquake focal mechanisms, *Phys. Earth planet. Inter.*, **75**, 193–198.
- Fukuyama, E., Ellsworth, W.L., Waldhauser, F. & Kubo, A., 2003. Detailed fault structure of the 2000 western Tottori, Japan, earthquake sequence, *Bull. seism. Soc. Am.*, **93**, 1468–1478.
- Gangopadhyay, A. & Talwani, P., 2003. Symptomatic features of intraplate earthquakes, *Seismol. Res. Lett.*, **74**, 863–883.
- Goebel, T.H.W., Becker, T.W., Schorlemmer, D., Stanchits, S., Sammis, C., Rybacki, E. & Dresen, G., 2012. Identifying fault heterogeneity through mapping spatial anomalies in acoustic emission statistics, *J. geophys. Res.*, **117**, B03310.
- Gomberg, J., Bodin, P. & Reasenberg, P.A., 2003. Observing earthquakes triggered in the near field by dynamic deformations, *Bull. seism. Soc. Am.*, **93**, 118–138.
- Grigoli, F., Cesca, S., Amoroso, O., Emolo, A., Zollo, A. & Dahm, T., 2013. Automated seismic event location by waveform coherence analysis, *Geophys. J. Int.*, **196**, 1742–1753.
- Han, M., Kim, K.H., Son, M. & Kang, S.Y., 2017. Current microseismicity and generating faults in the Gyeongju area, southeastern Korea, *Tectonophysics*, **694**, 414–423.
- Hardebeck, J.L. & Michael, A.J., 2006. Damped regional-scale stress inversions: methodology and examples for southern California and the Coalinga aftershock sequence, *J. geophys. Res.*, **111**, B11310.
- Hauksson, E. & Shearer, P., 2005. Southern California hypocenter relocation with waveform cross-correlation, Part 1: results using the double-difference method, *Bull. seism. Soc. Am.*, **95**, 896–903.
- Hong, T.-K., Lee, J., Kim, W., Hahm, I.-K., Woo, N.C. & Park, S., 2017. The 12 September 2016 M_L 5.8 midcrustal earthquake in the Korean Peninsula and its seismic implications, *Geophys. Res. Lett.*, **44**, 3131–3138.
- Hosono, K. & Yoshida, A., 2002. Do large aftershocks decrease similarly to smaller ones? *Geophys. Res. Lett.*, **29**, 120–120–4.
- Hwang, B.H., Son, M., Yang, K., Yoon, J. & Ernst, W.G., 2008. Tectonic evolution of the Gyeongsang Basin, southeastern Korea from 140 Ma to the present, based on a strike-slip and block rotation tectonic model, *Int. Geol. Rev.*, **50**, 343–363.
- Jaeger, J.C., Cook, N.G.W. & Zimmerman, R., 2009. *Fundamentals of Rock Mechanics*, p. 488, John Wiley & Sons.
- Johnston, A.C., 1989. The seismicity of 'stable continental interiors, in *Earthquakes at North-Atlantic Passive Margins: Neotectonics and Post-glacial Rebound*, pp. 299–327, ed. Gregersen, S. & Basham, P.W., Springer.
- Jolliffe, I., 2011. Principal component analysis, in *International Encyclopedia of Statistical Science*, pp. 1094–1096, Springer.
- Kim, K.-H. et al. 2016a. The 12 September 2016 Gyeongju earthquakes: 2. Temporary seismic network for monitoring aftershocks, *Geosci. J.*, **20**, 753–757.
- Kim, K.-H. et al. 2017a. Deep fault plane revealed by high-precision locations of early aftershocks following the 12 September 2016 M_L 5.8 Gyeongju, Korea, earthquake, *Bull. seism. Soc. Am.*, **108**, 517–523.
- Kim, S., Rhie, J. & Kim, G., 2011. Forward waveform modelling procedure for 1-D crustal velocity structure and its application to the southern Korean Peninsula, *Geophys. J. Int.*, **149**, 118–133.
- Kim, Y.-H., He, X., Ni, S., Lim, H. & Park, S.-C., 2017b. Earthquake source mechanism and rupture directivity of the 12 September 2016 Mw 5.5 Gyeongju, South Korea, earthquake, *Bull. seism. Soc. Am.*, **107**, 2525–2531.
- Kim, Y.-H., Rhie, J., Kang, T.-S., Kim, K.-H., Kim, M. & Lee, S.-J., 2016b. The 12 September 2016 Gyeongju earthquakes: 1. Observation and remaining questions, *Geosci. J.*, **20**, 747–752.
- Kim, Y.-S., Kim, T., Kyung, J.B., Cho, C.S., Choi, J.-H. & Choi, C.U., 2017c. Preliminary study on rupture mechanism of the 9.12 Gyeongju earthquake, *J. Geol. Soc. Korea*, **53**, 407–422 (in Korean).
- King, G.C., Stein, R.S. & Lin, J., 1994. Static stress changes and the triggering of earthquakes, *Bull. seism. Soc. Am.*, **84**, 935–953.

- Kyung, J.B., 2003. Paleoseismology of the Yangsan fault, south-eastern part of the Korean peninsula, *Ann. Geophys.*, **46**, 983–996.
- Lahr, J.C., 1999. HYPOELLIPSE: a computer program for determining local earthquake hypocentral parameters, magnitude, and first-motion pattern (Y2K compliant version), 1999 version 1.0, 119 pp., Open-File Report 99–23, U.S. Geol. Surv., Reston, VA.
- Lay, T. & Wallace, T.C., 1995. *Modern Global Seismology*, p. 521, Academic Press.
- Lee, J. *et al.* 2018. Seismicity of the 2016 M L 5.8 Gyeongju earthquake and aftershocks in South Korea, *Geosci. J.*, **22**, 433–444.
- Lee, K. & Jin, Y.G., 1991. Segmentation of the Yangsan Fault System: geophysical studies on major faults in the Kyeongsang Basin, *J. Geol. Soc. Korea*, **27**, 434–449.
- Lin, J. & Stein, R.S., 2004. Stress triggering in thrust and subduction earthquakes and stress interaction between the southern San Andreas and nearby thrust and strike-slip faults, *J. geophys. Res.*, **109**, B02303.
- Martínez-Garzón, P., Kwiątek, G., Ickrath, M. & Bohnhoff, M., 2014. MSATSI: a MATLAB package for stress inversion combining solid classic methodology, a new simplified user-handling, and a visualization tool, *Seismol. Res. Lett.*, **85**, 896–904.
- Matos, C., Custódio, S., Batlló, J., Zahradník, J., Arroucou, P., Silveira, G. & Heimann, S., 2018. An active seismic zone in intraplate west Iberia inferred from high resolution geophysical data, *J. geophys. Res.*, **123**, 2885–2907.
- Mendoza, C. & Hartzell, S. H., 1988. Aftershock patterns and main shock faulting, *Bull. seism. Soc. Am.*, **78**, 1438–1449.
- Meng, L., Ampuero, J.P., Stock, J., Duputel, Z., Luo, Y. & Tsai, V.C., 2012. Earthquake in a maze: compressional rupture branching during the 2012 Mw 8.6 Sumatra earthquake, *Science*, **337**, 724–726.
- Ogata, Y., 1983. Estimation of the parameters in the modified Omori formula for aftershock frequencies by the maximum likelihood procedure, *J. Phys. Earth*, **31**, 115–124.
- Park, S.C., Yang, H., Lee, D.K., Park, E.H. & Lee, W.J., 2018. Did the 12 September 2016 Gyeongju, South Korea earthquake cause surface deformation? *Geosci. J.*, **22**, 337–346.
- Rabak, I., Langston, C., Bodin, P., Horton, S., Withers, M. & Powell, C., 2010. The Enola, Arkansas, intraplate swarm of 2001, *Seismol. Res. Lett.*, **81**, 549–559.
- Rastogi, B.K. *et al.* 2001. The deadliest stable continental region earthquake occurred near Bhuj on 26 January 2001, *J. Seismol.*, **5**, 609–615.
- Raub, C., Martínez-Garzón, P., Kwiątek, G., Bohnhoff, M. & Dresen, G., 2017. Variations of seismic b-value at different stages of the seismic cycle along the North Anatolian Fault Zone in northwestern Turkey, *Tectonophysics*, **712**, 232–248.
- Reasenber, P.A. & Simpson, R.W., 1992. Response of regional seismicity to the static stress change produced by the Loma Prieta earthquake, *Science*, **255**, 1687–1690.
- Robinson, D.P., Henry, C., Das, S. & Woodhouse, J.H., 2001. Simultaneous rupture along two conjugate planes of the Wharton Basin earthquake, *Science*, **292**, 1145–1148.
- Ross, Z.E., Kanamori, H., Hauksson, E. & Aso, N., 2018. Dissipative intraplate faulting during the 2016 Mw 6.2 Tottori, Japan earthquake, *J. geophys. Res.*, **123**, 1631–1642.
- Schorlemmer, D., Wiemer, S. & Wyss, M., 2005. Variations in earthquake-size distribution across different stress regimes, *Nature*, **437**, 539–542.
- Shcherbakov, R., Turcotte, D.L. & Rundle, J.B., 2006. Scaling properties of the Parkfield aftershock sequence, *Bull. seism. Soc. Am.*, **96**, S376–S384.
- Shelly, D.R., Ellsworth, W.L. & Hill, D.P., 2016. Fluid-faulting evolution in high definition: connecting fault structure and frequency-magnitude variations during the 2014 Long Valley Caldera, California, earthquake swarm, *J. geophys. Res.*, **121**, 1776–1795.
- Shi, Y. & Bolt, B.A., 1982. The standard error of the magnitude-frequency b value, *Bull. seism. Soc. Am.*, **72**, 1677–1687.
- Snoke, J.A., 2003. FOCMEC: focal mechanism determinations, in *International Handbook of Earthquake and Engineering Seismology*, Chapter 85.12, pp. 1629–1630, eds Lee, W.H.K., Kanamori, H., Jennings, P.C. & Kisslinger, C., Academic Press.
- So, M.M.L., Mote, T. & Pappin, J.W., 2016. Seismic hazard assessment of South Korea, *Jpn. Geotech. Soc. Spec. Pub.*, **2**, 755–760.
- Soh, I., Chang, C., Lee, J., Hong, T.K. & Park, E.S., 2018. Tectonic stress orientations and magnitudes, and friction of faults, deduced from earthquake focal mechanism inversions over the Korean Peninsula, *Geophys. J. Int.*, **213**, 1360–1373.
- Sokos, E.N. & Zahradník, J., 2008. ISOLA a Fortran code and a Matlab GUI to perform multiple-point source inversion of seismic data, *Comput. Geosci.*, **34**, 967–977.
- Son, M., Cho, C.S., Shin, J.S., Rhee, H.M. & Sheen, D.H., 2017. Spatiotemporal distribution of events during the first three months of the 2016 Gyeongju, Korea, earthquake sequence, *Bull. seism. Soc. Am.*, **108**, 210–217.
- Soto-Cordero, L., Meltzer, A. & Stachnik, J.C., 2018. Crustal structure, intraplate seismicity, and seismic hazard in the Mid-Atlantic United States, *Seismol. Res. Lett.*, **89**, 241–252.
- Sykes, L.R., 1978. Intraplate seismicity, reactivation of preexisting zones of weakness, alkaline magmatism, and other tectonism postdating continental fragmentation, *Rev. Geophys.*, **16**, 621–688.
- Talwani, P., 2014. Unified model for intraplate earthquakes, in *Intraplate Earthquakes*, pp. 275–327, ed. Talwani, P., Cambridge University Press.
- Talwani, P. & Rajendran, K., 1991. Some seismological and geometric features of intraplate earthquakes, *Tectonophysics*, **186**, 19–41.
- Tavakoli, B., Pezeshk, S. & Cox, R.T., 2010. Seismicity of the New Madrid seismic zone derived from a deep-seated strike-slip fault, *Bull. seism. Soc. Am.*, **100**, 1646–1658.
- Toda, S., Stein, R.S., Richards-Dinger, K. & Bozkurt, S.B., 2005. Forecasting the evolution of seismicity in southern California: animations built on earthquake stress transfer, *J. geophys. Res.*, **110**, B05S16.
- Tormann, T., Wiemer, S. & Mignan, A., 2014. Systematic survey of high-resolution b value imaging along Californian faults: inference on asperities, *J. geophys. Res.*, **119**, 2029–2054.
- Uchide, T. & Song, S.G., 2018. Fault rupture model of the 2016 Gyeongju, South Korea, earthquake and its implication for the underground fault system, *Geophys. Res. Lett.*, **45**, 2257–2264.
- Utsu, T., 1992. On seismicity, in mathematical seismology (VII), *Coop. Res. Rep. Inst. Stat. Math., Tokyo*, **34**, 139–157.
- Utsu, T. & Ogata, Y., 1995. The centenary of the Omori formula for a decay law of aftershock activity, *J. Phys. Earth*, **43**, 1–33.
- Waldhauser, F. & Ellsworth, W.L., 2000. A double-difference earthquake location algorithm: method and application to the northern Hayward Fault, California, *Bull. seism. Soc. Am.*, **90**, 1353–1368.
- Wang, Z., 2007. Seismic hazard and risk assessment in the intraplate environment: the New Madrid seismic zone of the central United States, *Geol. Soc. Am.*, **425**, 363–373.
- Westerhaus, M., Wyss, M., Yilmaz, R. & Zschau, J., 2002. Correlating variations of b values and crustal deformations during the 1990s may have pinpointed the rupture initiation of the M w = 7.4 Izmit earthquake of 1999 August 17, *Geophys. J. Int.*, **148**, 139–152.
- Wiemer, S. & Katsumata, K., 1999. Spatial variability of seismicity parameters in aftershock zones, *J. geophys. Res.*, **104**, 13 135–13 151.
- Wiemer, S. & Wyss, M., 2000. Minimum magnitude of completeness in earthquake catalogs: examples from Alaska, the western United States, and Japan, *Bull. seism. Soc. Am.*, **90**, 859–869.
- Withers, M., Aster, R., Young, C., Beiriger, J., Harris, M., Moore, S. & Trujillo, J., 1998. A comparison of select trigger algorithms for automated global seismic phase and event detection, *Bull. seism. Soc. Am.*, **88**, 95–106.
- Woo, J.U., Kim, J., Rhie, J. & Kang, T.S., 2017. Characteristics in hypocenters of microseismic events due to hydraulic fracturing and natural faults: a case study in the Horn River Basin, Canada, *Geosci. J.*, **21**, 683–694.
- Wu, Q., Chapman, M.C. & Beale, J.N., 2015. The aftershock sequence of the 2011 Mineral, Virginia, earthquake: temporal and spatial distribution,

- focal mechanisms, regional stress, and the role of Coulomb stress transfer, *Bull. seism. Soc. Am.*, **105**, 2521–2537.
- Yano, T.E. & Matsubara, M., 2017. Effect of newly refined hypocenter locations on the seismic activity recorded during the 2016 Kumamoto Earthquake sequence, *Earth, Planets Space*, **69**, 74.
- Zhao, Y.Z. & Wu, Z.L., 2008. Mapping the b–values along the Longmenshan fault zone before and after the 12 May 2008, Wenchuan, China, Ms 8.0 earthquake, *Nat. Hazards Earth Syst. Sci.*, **8**, 1375–1385.
- Zoback, M.L., 1992. First- and second-order patterns of stress in the lithosphere: the world stress map project, *J. geophys. Res.*, **97**, 11 703–11 728.